Surface Flux Variability over the North Pacific and North Atlantic Oceans

MICHAEL A. ALEXANDER AND JAMES D. SCOTT

CIRES, University of Colorado, Boulder, Colorado

(Manuscript received 22 January 1996, in final form 9 May 1997)

ABSTRACT

Daily fields obtained from a 17-yr atmospheric GCM simulation are used to study the surface sensible and latent heat flux variability and its relationship to the sea level pressure (SLP) field. The fluxes are analyzed over the North Pacific and Atlantic Oceans during winter. The leading mode of interannual SLP variability consists of a single center associated with the Aleutian low in the Pacific, and a dipole pattern associated with the Icelandic low and Azores high in the Atlantic. The surface flux anomalies are organized by the low-level atmospheric circulation associated with these modes in agreement with previous observational studies.

The surface flux variability on all of the timescales examined, including intraseasonal, interannual, 3–10 day, and 10–30 day, is maximized along the north and west edges of both oceans and between Japan and the date line at ~35°N in the Pacific. The intraseasonal variability is approximately 3–5 times larger than the interannual variability, with more than half of the total surface flux variability occuring on timescales of less than 1 month. Surface flux variability in the 3–10-day band is clearly associated with midlatitude synoptic storms. Composites indicate upward (downward) flux anomalies that exceed $|30\ \mathrm{W\ m^{-2}}|$ occur to the west (east) of storms, which move eastward across the oceans at 10°–15° per day. The SLP and surface flux anomalies are also strong and coherent in the 10–30-day band but are located farther north, are broader in scale, and propagate ~3–4 times more slowly eastward than the synoptic disturbances.

The sensible and latent heat flux are proportional to the wind speed multiplied by the air–sea temperature and humidity difference, respectively. The anomalous wind speed has the greatest influence on surface flux anomalies in the subtropics and western Pacific, while the air temperature and moisture anomalies have the greatest impact in the northeast Pacific and north of 40°N in the Atlantic. The covariance between the wind speed and the air temperature or humidity anomalies, while generally small, is nonnegligible on synoptic timescales.

1. Introduction

Fluxes of energy, momentum, and moisture across the air–sea interface play an integral role in the earth's climate. For example, the mean upper ocean circulation is primarily driven by the winds, while evaporation from the sea surface and the resulting release of latent heat drives much of the atmospheric circulation. In midlatitudes, the largest energy exchanges across the air–sea interface occur during winter through the fluxes of sensible and latent heat. These fluxes depend on the near-surface wind speed, temperature, and humidity fields, all closely associated with the atmospheric circulation, and the sea surface temperature (SST). Most studies have shown that the atmosphere governs the surface flux variability on subdecadal timescales. In this study, we will explore the relationship between the sensible and latent heat flux and the atmospheric circulation over the Northern Hemisphere oceans during and between winters.

Many studies of midlatitude air–sea interaction (e.g., Kraus and Morrison 1966; Elsberry and Camp 1978; Gulev 1997) utilized data collected at ocean weather stations (OWSs) scattered over the North Atlantic and North Pacific, one of the few sources of long-term data records over the oceans. Zhao and McBean (1986) and Cayan (1992) were among the first to examine basin-wide surface flux variability and the processes that generate this variability over the oceans. They used monthly averaged data to investigate the spatial variability of the fluxes, and their relationship to the atmospheric circulation and sea surface temperature (SST) anomalies. Using principal component analyses and canonical correlations, Cayan (1992) found that the interannual variability in the surface fluxes is closely linked to the dominant patterns of atmospheric circulation over the North Atlantic and North Pacific Oceans. These heat flux anomalies then force SST anomalies to form, resulting in the tendency of the SST anomaly fields to closely match the heat flux anomaly patterns. Cayan's results were confirmed by Iwasaka and Wallace (1995), who applied singular value decomposition (SVD) to paired fields of 500-mb height, surface fluxes, and SST tendency.

Corresponding author address: Dr. Michael A. Alexander, CIRES, University of Colorado, Box 449, Boulder, CO 80309.
E-mail: maa@cdc.noaa.gov

In contrast to the limited number of papers on basin-scale, low-frequency, surface flux variability, there have been numerous studies of the relationship between midlatitude cyclones and oceanic surface fluxes. Petterssen et al. (1962) constructed composites of midlatitude cyclones in various stages of development over the North Atlantic and found large upward heat fluxes in the cold sector west of the storm's center. Recent studies have shown that the sensible plus latent heat flux can exceed 2000 W m^{-2} in the cold sector of strong storms (Neiman and Shapiro 1993). Sanders and Gyakum (1980), Sanders (1986), Monobianco (1989), plus many more have examined ''bombs''—midlatitude cyclones that develop rapidly over the ocean. These storms preferentially develop over regions of strong SST gradients, such as the one associated with the Gulf Stream, where surface fluxes destabilize the atmosphere and increase the low-level baroclinicity. In model simulations of bombs performed with and without surface fluxes, some have indicated that the fluxes had little impact on storm development (Chang et al. 1989; Kuo and Low-Nam 1990). Other studies found that the flux of heat into in the cold sector of the storm reduced the low-level baroclinicity, decreasing the storm's intensity (Nuss and Anthes 1987; Reed and Simmons 1991). However, it appears surface fluxes play an important role in preconditioning the atmosphere for rapid cyclogenesis. Modeling studies by Uccellini et al. (1987), Nuss (1989), and Kuo et al. (1991) indicate that surface fluxes enhance the potential for rapid storm development in the precylogenesis stage by increasing the available moisture, enhancing the low-level baroclinicity associated with coastal fronts, and reducing the static stability.

On synoptic timescales, surface fluxes not only supply energy for cyclone development but can also force SSTs to change rapidly. Using data from OWSs and one-dimensional mixed layer model simulations Camp and Elsberry (1978), Davis et al. (1981), and Large et al. (1994) showed that the SST cooled by more than 1°C within days of the passage of storms through increased surface heat fluxes and turbulent mixing within the ocean. The latter enhances the entrainment of cold water from the deeper ocean into the surface layer. Frankignoul and Hasselmann (1977), Frankignoul and Reynolds (1983), Alexander and Penland (1996), Hall and Manabe (1996), and Halliwell and Mayer (1996) have shown that outside of regions with strong currents, much of the variability of SST anomalies can be explained by the integrated effect of surface forcing due to storms damped by negative air-sea feedback. The rapid decorrelation time between synoptic events results in a nearly uniform or ''white'' spectrum of the surface forcing over the periods at which SST anomalies evolve. The thermal damping occurs as anomalously warm (cold) water loses more (less) heat to the atmosphere, which causes SST anomalies to decay with an *e*-folding time of 3–6 months. This framework for midlatitude air–sea interaction can be used to explain why the dominant large-scale patterns of SST anomalies are associated with regions of large submonthly atmospheric variability (Zorita et al. 1992; Gulev 1997) and why the SST anomalies reach a maximum ~2–3 weeks after the peak atmospheric forcing has occurred (Deser and Timlin 1997).

The structure of atmospheric variability depends on timescale, even at periods of less than 1 month. Synoptic variability associated with midlatitude storms occurs on timescales of approximately 2–10 days (Blackmon et al. 1977; Wallace et al. 1988). Rossby waves, blocking events, slowly moving cutoff lows, and semistationary patterns (Blackmon et al. 1984; Kushnir and Wallace 1989; Dole and Black 1990; Lanzante 1990) all contribute to atmospheric variability at lower frequencies, especially timescales of 10–30 days. It is thus natural to inquire how the surface fluxes are organized at these two different timescales.

Sensible (latent) heat flux anomalies depend on the product of the mean air–sea temperature (moisture) difference times the anomalous wind speed and vice versa; thus, the mean climatological state can strongly influence the surface fluxes anomalies. Some studies have found that SST anomalies are driven by fluctuations in the air temperature and humidity, rather than wind speed (Luksch and von Storch 1992; Battisti et al. 1995; Lau and Nath 1996), while others have indicated that SST anomalies are closely tied to wind speed fluctuations (O'Brien and Chassignet 1995; Halliwell and Mayer 1996; Halliwell 1997). Cayan (1992) found that the sensible heat flux is primarily controlled by air temperature anomalies while the latent heat flux is influenced by both wind and moisture anomalies, though the relative contributions of these variables to the flux anomalies varied over the North Pacific and Atlantic Oceans. In addition, Halliwell (1997) noted that the relative influence of wind speed and air temperature anomalies on the ocean may be timescale dependent since the air temperature comes into thermal balance with the underlying SST over longer periods.

General circulation models (GCMs) of the atmosphere, ocean, and the two systems coupled together have been used to study the atmospheric response to SST anomalies, the development of ocean temperature anomalies in response to atmospheric forcing, and the coevolution of anomalies in both systems. However, a detailed analysis of surface fluxes in GCMs has not yet been performed. GCMs have the benefit that variables can be obtained at each grid point over the entire domain on relatively short timescales and that the model fields are in dynamic and thermodynamic balance. The model's fidelity can be benchmarked by comparing its representation of the surface flux variability and low-level atmospheric circulation to observations.

Here we examine a 17-yr simulation performed with the Geophysical Fluid Dynamics Lab (GFDL) GCM, described in section 2, to examine the temporal and spatial variability of surface fluxes over the North Pa-

cific and Atlantic Oceans with the aim of bridging the gap between previous studies of interannual variability and those that have focused on the fluxes associated with storms. The SST and sea ice boundary conditions in the model simulation repeat the same seasonal cycle each year, thus we can isolate the surface flux variability, which is independent from oceanic fluctuations. In section 3, we investigate the relationship between the near-surface atmospheric circulation and the surface fluxes, the timescale dependence of the surface fluxes, and the relative contribution of the wind speed, air temperature, and humidity to the surface flux variability. The results, including differences in the surface flux characteristics over the Atlantic and Pacific Oceans, are summarized and discussed in section 4.

2. The GFDL GCM and processing of model fields

The atmospheric GCM used in this study is a global spectral model with rhomboidal truncation at wavenumber 30, corresponding to a horizontal resolution of approximately 2.25° latitude × 3.75° longitude. There are 14 unequally spaced sigma levels in the vertical, with the lowest level at ~30 m above the surface. The GCM was integrated for 17 yr, in which the mean seasonal cycle of SST and sea ice, derived from long term climatologies, were repeated each year. The model includes smoothed orography, gravity wave drag, and predicted clouds. Stratiform clouds form and precipitation begins when the relative humidity exceeds 100%, while subgrid-scale precipitation is parameterized by moist convective adjustment. Soil moisture is predicted using the bucket method, where the ground can absorb up to 1.5 m of precipitation before runoff begins. Many features of the model's climate from this simulation are presented in a printed atlas and an electronic version on the World Wide Web (Alexander and Scott 1995, 1996a), while a more complete description of an earlier version of the GCM is given by Gordon and Stern (1982) and Manabe and Hahn (1981).

The model's surface sensible and latent heat flux are computed using standard bulk aerodynamic formulas:

$$Q_{\rm sh} = c_p c_H \rho U(SST - T_{\rm air}) \quad (1)$$

$$Q_{\rm lh} = c_e L \rho U(q_{\rm sat} - q_{\rm air}), \quad (2)$$

where c_p and ρ are the specific heat and density of air; L is the latent heat of vaporization; c_H and c_e are the heat and moisture flux coefficients, which are both assigned a constant value of 1×10^{-3}; U is the wind speed; $T_{\rm air}$ and $q_{\rm air}$ are the air temperature and specific humidity at the lowest model level; and $q_{\rm sat}$ is the saturation specific humidity, which is solely a function of SST. The mean sum of the sensible and latent heat flux ($Q_{\rm sh} + Q_{\rm lh}$) in the GFDL GCM closely matches that obtained from the National Center for Environmental Prediction (NCEP) Re-analysis Project with upward heat fluxes exceeding 300 W m^{-2} just east of Asia during winter (Alexander and Scott 1996b).

Relationships between anomalies in $Q_{\rm sh}$ and $Q_{\rm lh}$ and those in wind speed air temperature and humidity are examined in section 3c, so it is important to note that the values of $Q_{\rm sh}$ and $Q_{\rm lh}$ archived directly from the model do not exactly match those computed off-line using the archived values of U, $T_{\rm air}$, and $q_{\rm air}$ in (1) and (2). This discrepancy appears to occur for two reasons. First, processes that alter the atmospheric variables, such as radiation and convection, are executed in the subroutine calling sequence after the fluxes have already been computed. Second, while both the surface fluxes and atmospheric variables are archived every 24 h, $Q_{\rm sh}$ and $Q_{\rm lh}$ are stored as daily averages, while U, $T_{\rm air}$, and $q_{\rm air}$ are stored as instantaneous values from one model time step. We infer that processes such as convection, which mix heat upward and momentum downward into the surface layer in winter, reduce $T_{\rm air}$ and $q_{\rm air}$ and enhance U, thereby, increasing the mean upward heat flux in the off-line calculations, while time averaging suppresses the variance of the archived flux values. As a result, $Q_{\rm sh}$ and $Q_{\rm lh}$ computed off-line, using the primary variables have means (standard deviations) that are approximately 20% (30%–50%) larger than the archived flux values during winter, though the patterns of variability are similar.

We perform analyses using daily values of the surface sensible and latent heat flux and the low-level atmospheric fields during the months of December, January, and February (DJF).[1] Daily anomalies are computed from the daily values minus the long-term DJF (monthly) mean in section 3a (3b and 3c). In some analyses, the daily anomalies are time filtered using a Lanczos filter (Duchon 1979) to isolate synoptic (3–10-day) and lower-frequency (10–30-day) variability. Filtering is performed using 121 weights, requiring 60 days of data on either side of the time point being filtered including values prior to December and after February. We also examine the interannual (winter-to-winter) variability, the departure of the mean for a particular DJF season from the long-term DJF mean, and the intraseasonal (within winter) variability, the departure of the daily values from the mean of that one season. The sum of the intraseasonal and interannual variance equals the total variance of the daily anomalies during the 16 available DJF periods. The variability of the model's sensible and latent heat flux and the relationship to the low-level atmospheric fields are examined using empirical orthogonal functions (EOFs), standard deviations, lead-lag correlations, composites, and regressions.

[1] The shortwave and longwave radiation, the other two terms in the surface energy budget, are archived as monthly averages. They are believed to play a secondary role in the surface energy balance over most of the midlatitudes during winter and will not be discussed here.

3. Results

a. Interannual and intraseasonal variability

As a first step, we examine the relationship between the dominant patterns of sea level pressure (SLP) and surface flux variability on interannual timescales in the GFDL GCM; the results will then be compared to previous observational studies. The first EOF of SLP over the North Pacific (Fig. 1a) explains 58% of the winter-to-winter variance and has one main center that extends across the basin at 45°N. This mode is associated with changes in strength and position of the Aleutian low. When the low is stronger than normal (the positive phase of EOF 1), the associated cyclonic circulation (assuming the flow is nearly geostrophic) results in stronger winds and colder air flowing out over the western Pacific, while warm moist air is advected northward in the northeast part of the basin. This circulation pattern suggests enhanced heat loss from the ocean to the atmosphere in the central and west Pacific, while the ocean heat loss is reduced off the coast of North America and in the Gulf of Alaska. EOF 1 of $Q_{sh} + Q_{lh}$ (Fig. 1b), which explains 43% of the variance, has this pattern with anomalies of one sign between 30° and 45°N from Japan to 140°W, and anomalies of the opposite sign to the north and east. The relationship between the leading SLP and $Q_{sh} + Q_{lh}$ EOF patterns is examined more rigorously by computing the correlation between the first principal component (PC 1) of SLP, the time series corresponding to EOF 1, with the $Q_{sh} + Q_{lh}$ anomalies at each model grid point over the North Pacific (Fig. 1c). The pattern closely resembles the first EOF of $Q_{sh} + Q_{lh}$ (Fig. 1b) with the magnitude of the correlations exceeding 0.6 over much of the central and east Pacific.

EOF 1 of SLP and $Q_{sh} + Q_{lh}$, and the correlation of SLP PC 1 with $Q_{sh} + Q_{lh}$ anomalies over the North Atlantic are presented in Fig. 2. In contrast to the Pacific, the leading SLP anomaly pattern is a dipole with one center east of Iceland and the second in the central North Atlantic. The implied zonal circulation associated with the dipole SLP mode would lead to bands of anomalous surface fluxes, with a node at ~42°N as seen in Fig. 2a,b. However, the change in sign of the flux anomalies between 25°–35°N is not accompanied by a reversal in direction of the anomalous flow as indicated by the SLP gradient in Fig 2a. In this region the mean circulation switches from midlatitude westerlies to subtropical easterlies, so a zonal wind anomaly that would enhance the wind speed and the advection of continental air over the ocean at 35°N would have the opposite affect at 25°N, resulting in flux anomalies of opposite sign. Here, EOF 1 of $Q_{sh} + Q_{lh}$ (Fig. 2b) and the correlation between PC 1 of SLP and the grid point values of $Q_{sh} + Q_{lh}$ (Fig. 2c) both indicate the dominant pattern of surface flux variability consists of zonal bands with nodes at ~25° and ~45°N that are linked to the anomalous near-surface atmospheric circulation.

The link between SLP and $Q_{sh} + Q_{lh}$ for the winter season has been examined further using SVD analyses, which maximizes the covariance between two fields (Bretherton et al. 1992). The first mode dominates the covariability between the SLP and $Q_{sh} + Q_{lh}$ fields over the North Pacific and North Atlantic Oceans, explaining more than three-fourths of the squared covariance over both ocean basins. Maps of heterogeneous correlations between the two fields for the leading mode (not shown), one method of displaying the SVD results, are very similar to those based on observations (Iwasaka and

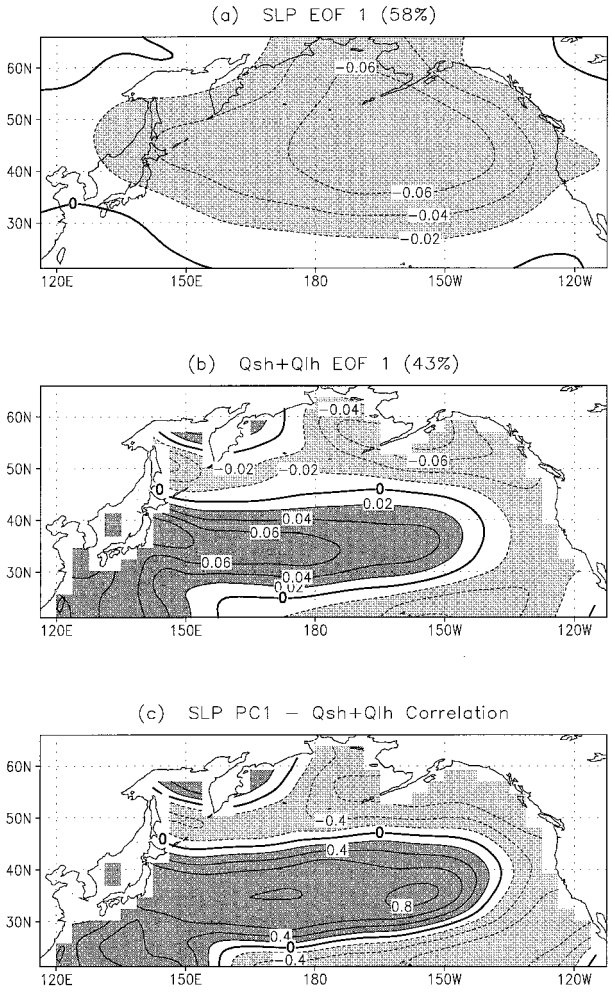

FIG. 1. EOF 1 of interannual (a) SLP and (b) $Q_{sh} + Q_{lh}$ anomalies over the North Pacific, based on departures of individual DJF means from the 16-yr DJF mean, and (c) the correlation between PC 1 of SLP, the time series associated with (a), and gridpoint values of $Q_{sh} + Q_{lh}$. EOF 1 explains 58% (43%) of the SLP ($Q_{sh} + Q_{lh}$) variance. The contour interval is 0.02 in (a) and (b) and 0.2 in (c). Negative contours are dashed, and values greater (less) than +1 (−1) contour interval are shaded dark (light). Upward-directed flux anomalies are positive. EOFs are computed using the covariance matrix and the resulting fields normalized so the sum of the squares of the gridpoint values equal one. The fields input into the EOF analyses are the actual values from the model's Gaussian grid; cosine weighting the fields by latitude gave similar results but with the patterns shifted slightly to the south.

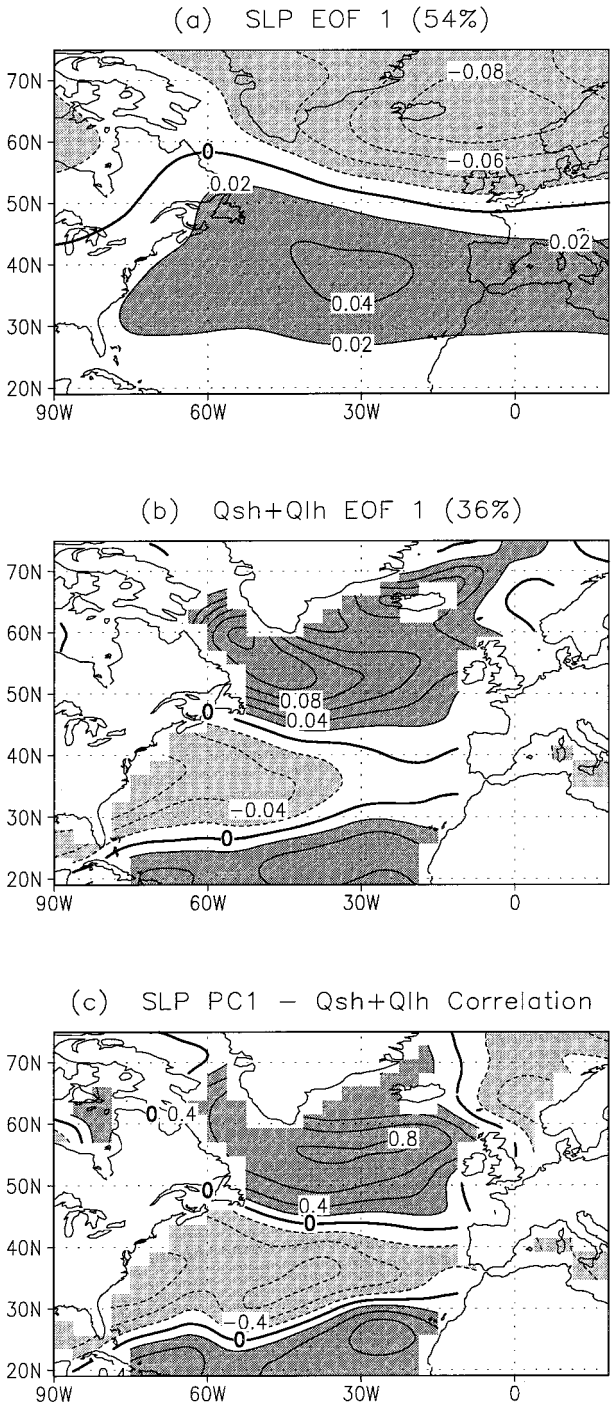

FIG. 2. EOF 1 of interannual (a) SLP and (b) $Q'_{sh} + Q_{lh}$ anomalies over the North Atlantic and (c) the correlation between PC 1 of SLP and grid-point values of $Q'_{sh} + Q'_{lh}$. EOF 1 explains 54% (36%) of the SLP ($Q_{sh} + Q_{lh}$) variance. Contour interval and shading as in Fig. 1.

Wallace 1995) and to the EOF and correlation maps presented in Figs. 1 and 2.

The relationship between the SLP and the surface heat fluxes on interannual timescales obtained from the GFDL GCM agree well with the observational studies

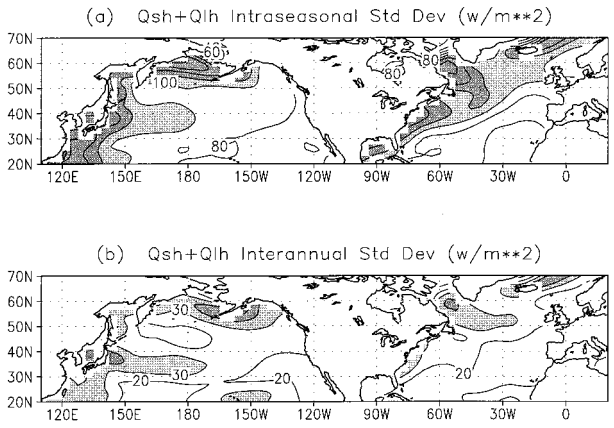

FIG. 3. The standard deviation of (a) intraseasonal and (b) interannual $Q_{sh} + Q_{lh}$ anomalies, based on departures within and between DJF periods. Contour interval is 20 W m^{-2} in (a) and 10 W m^{-2} in (b); values between 100–120 and (a) and 30–40 in (b) are shaded light, while those greater than 120 in (a) and 40 in (b) are shaded dark.

of Cayan (1992a, b) and Iwasaka and Wallace (1995) in that i) the leading patterns of SLP and surface flux variability in the model and observations are similar, ii) the SLP patterns resemble the oceanic portion of the North Atlantic Oscillation and the Pacific North American pattern, iii) the surface flux variability is regulated by the low-level atmospheric circulation, iv) the percent variance explained by EOF 1 of SLP exceeds that of $Q_{sh} + Q_{lh}$ since the surface flux variability is not as spatially coherent, and v) the maxima in the pressure and pressure gradients are located over the central portion of both the Atlantic and Pacific while the surface flux maxima are found near continents, primarily on the western side of the basins. The circulation and surface flux anomalies are not necessarily collocated because the latter also depends on the air–sea temperature and humidity differences, which are greatest just east of the continents. The model's ability to reproduce the observed characteristics of the surface fluxes on interannual timescales indicates that the leading patterns of variability during winter are not critically dependent on SST anomalies, which are not included in this GCM simulation, and also gives us some confidence to investigate the model's surface flux variability on intraseasonal timescales.

The standard deviation (σ) of $Q_{sh} + Q_{lh}$ on intraseasonal (Fig. 3a) and interannual (Fig. 3b) timescales, $\overline{u}_{sea}$ and $\overline{v}_{ann}$, which represent the variability within and between DJF periods, have very similar patterns. In the Pacific, σ_{sea} and σ_{ann} maxima are found along the coast and extend eastward between 20°–25°N, 35°–45°N, and 50°–60°N reaching about 150°E, 180°, and 140°W, respectively. In the Atlantic, the largest standard deviations on both timescales extend northeastward, paralleling the coasts of the North America and Greenland with pronounced maxima over the Labrador Sea, and from Greenland east to the Norwegian Sea. The σ_{sea}

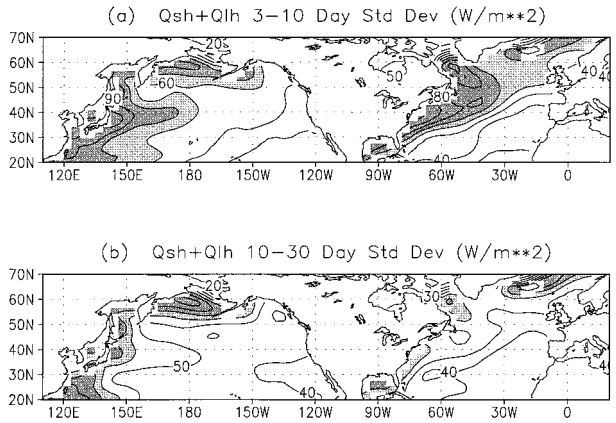

FIG. 4. The standard deviation of $Q_{sh} + Q'_{lh}$ ($'$ denotes daily anomalies), which have been filtered to retain timescales of (a) 3–10 and (b) 10–30 days. Contour interval is 10 W m^{-2} and values between 60–70 are shaded light, while those greater than 70 W m^{-2} are shaded dark.

values exceed 100 W m^{-2} over ~one-third of the domain, and are generally 3–5 times larger than the σ_{ann} values, in agreement with Cayan (1992).

An explanation for why the standard deviation on interannual timescales are collocated with those on intraseasonal timescales but less than one-third as large may be that variability in both time bands are governed by flux anomalies that are nearly white in time and result from the passage of midlatitude storms. If $Q_{sh} + Q_{lh}$ variability is dominated by synoptic disturbances that have a Gaussian distribution and a short autocorrelation time (τ), that is, $Q_{sh} + Q_{lh}$ is white, for τ-day means then $\sigma_{ann} \sim \sigma_{sea}/\sqrt{90/\tau}$, where 90 is the number of days in DJF. Using typical τ values for $Q_{sh} + Q'_{lh}$ of 4 to 10 days (Frankignoul and Hasselmann 1977; Deser and Timlin 1997) results in $\sigma_{sea}/\sigma_{ann} \sim 3.0$–4.8, consistent with what is seen in Fig. 3.

b. Variability on timescales of 3–10 and 10–30 days

The standard deviation of the time filtered daily $Q_{sh} + Q_{lh}$ anomalies for periods of 3–10 and 10–30 days are presented in Fig. 4. Daily anomalies (denoted by primes) were first filtered over all but the first and final 60 days of the model simulation and the resulting timeseries were then used to compute σ during the 16 DJF periods. The pattern of the flux variability in the two time bands are similar over both the North Atlantic and North Pacific, with σ exceeding 60 W m^{-2} on the northwest side of both basins. The magnitude of σ in the synoptic (3–10-day) band tends to be slightly larger than that in the lower-frequency (10–30-day) band except over the eastern subtropics and parts of the northern edge of the domain. Fluctuations of $Q'_{sh} + Q'_{lh}$ in the 3–10- (10–30-) day band explain 30%–45% (20%–35%) of the total variance (not shown); thus, more than half of the DJF surface heat flux variability occurs at submonthly frequencies over almost all of the midlatitude oceans.

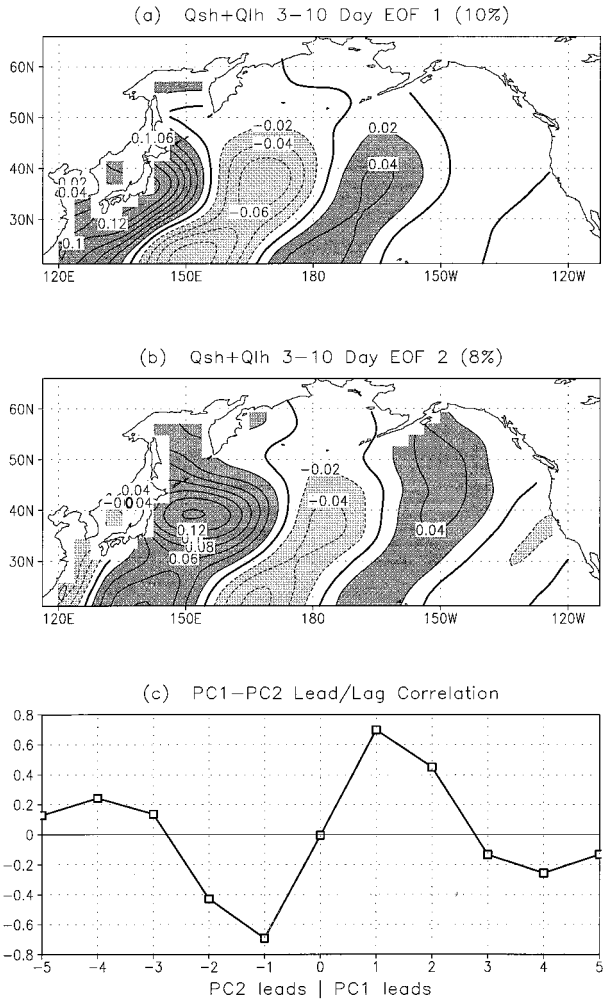

FIG. 5. The (a) first and (b) second EOF of daily $Q'_{sh} + Q'_{lh}$ over the North Pacific, which have been filtered to retain timescales of 3–10 days, and (c) the correlation between PC 1 and 2 in the 3–10-day band at lags of up to ±5 days. EOF 1 (2) explains 10% (8%) of the variance in the 3–10-day band. Contour interval and shading as in Fig. 1.

The spatial structures associated with synoptic surface flux variability are obtained from the leading pair of EOFs of $Q'_{sh} + Q'_{lh}$ filtered to retain periods of 3–10 days. The first two EOFs over the North Pacific (Fig. 5) are composed of a series of 4 to 5 individual anomaly centers that alternate in sign and together span most of the Pacific. The magnitude of the anomalies tends to be largest south of ~45°N and decreases from west to east across the basin. The individual anomalies, which slope toward the southwest south of 45°N, subtend ~25° of longitude and cover the entire meridional extent of the domain. The anomaly centers in EOF 2 are 20°–30° of longitude east of anomalies of the same sign in EOF 1. The two leading EOFs have a similar structure but appear to be in quadrature; that is, the anomaly maxima

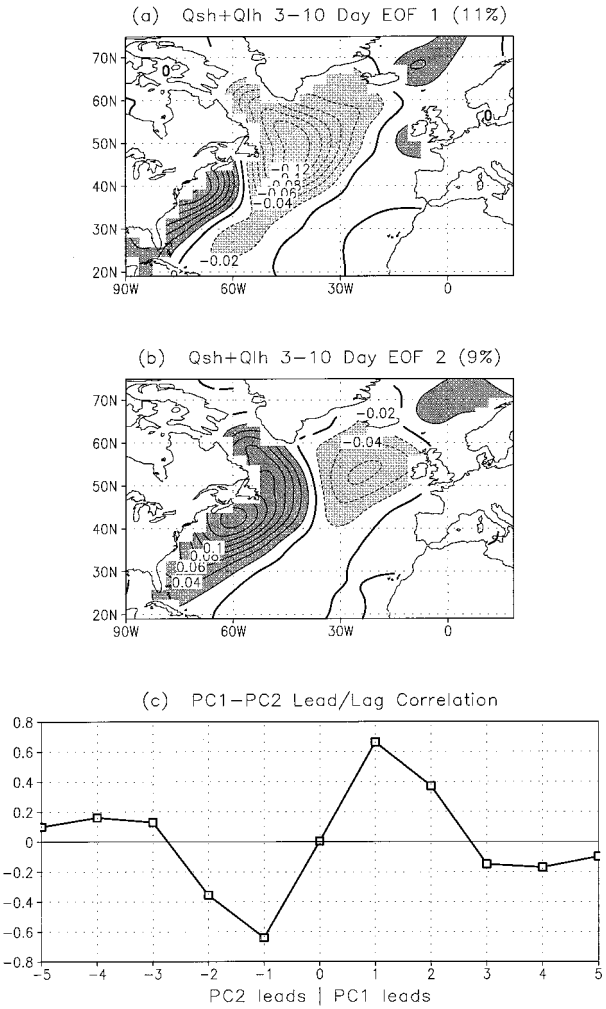

FIG. 6. The (a) first and (b) second EOF of daily $Q_{sh} + Q'_{lh}$ over the North Atlantic filtered to retain timescales of 3–10 days and (c) the correlation between PC 1 and 2 in the 3–10-day band at lags of up to ±5 days. EOF 1 (2) explains 11% (8%) of the variance. Contour interval and shading as in Fig. 1.

in EOF 1 coincide with the zero lines in EOF 2. Lead-lag correlations between the PCs corresponding to the two leading EOFs (Fig. 5c) is greater than 0.6 (less than −0.6) when PC 1 leads (lags) PC 2 by 1 day. Given that the first two EOFs explain a similar amount of variance (~10%), their spatial and temporal relationship suggests that the anomaly pattern shifts eastward over the Pacific by about 10°–15° day^{-1}.

The first two EOFs of the 3–10-day filtered $Q'_{sh} + Q'_{lh}$ over the Atlantic and the lead-lag correlation between their corresponding time series are shown in Fig. 6. Both EOFs have three centers, which lie along a southwest–northeast axis that extends across the basin. The anomalies have maximum amplitude off the east coast of the United States and over the Labrador Sea and the adjoining North Atlantic. As in the Pacific, the leading pair of patterns each explain ~10% of the variance, are in quadrature, and their time series are highly correlated when separated by 1 day, suggesting northeastward propagation of the anomaly pattern.

It is also possible to compute EOFs of the fluxes in the 3–10-day time band by first filtering the basic atmospheric variables and then using the filtered variables in the bulk formula to obtain Q'_{sh} and Q_{lh}. When the variables are filtered first, the leading EOF of $Q'_{sh} + Q'_{lh}$, which only explains ~5% of the variance, consists of one elongated band that extends from south of Japan to the central Pacific, diminishing as it crosses the basin (not shown). The second EOF is not paired with the first. It appears that by filtering the variables first, one obtains the surface flux anomalies associated with the overall storm track rather than individual storms. The covariance between U' and T'_{air} and U' and q'_{air} contribute to lower-frequency flux anomalies, as indicated by greater lag autocorrelations of PC 1, obtained from $Q'_{sh} + Q'_{lh}$ calculated with the filtered atmospheric variables, compared with those obtained when the fluxes were directly filtered (not shown).

We have also examined the standard deviation, the percent variance explained, and the two leading EOFs of SLP, in the 3–10-day band over the Northern Oceans during DJF (not shown). In agreement with previous analyses (Blackmon et al. 1977; Whittaker and Horn 1983; Wallace et al. 1988) strong synoptic variability occurs over the far North Pacific and Atlantic Oceans, coincident with the Aleutian and Iceland lows. While the anomalies of largest magnitude occur between 45°–65°N in the eastern half of both basins the percent variance explained by the 3–10-day band reaches a maximum over the western third of the oceans between 30° and 45°N. The EOF analyses of SLP indicates that the leading pair of patterns represent midlatitude storms that propagate eastward across the oceans in about 6 days.

The low-level atmospheric circulation and its relation to the surface fluxes on synoptic timescales is examined by compositing the 3–10-day filtered SLP′ and $Q'_{sh} + Q'_{lh}$ over the North Pacific and Atlantic Oceans when the filtered SLP at a selected basepoint is less than -1σ. In the Pacific, the basepoint is centrally located at 37°N and the dateline, where σ of SLP′ in the 3–10-day band is 6.0 mb. Composites based on an average of 207 cases are constructed at 0 lag (the reference time when SLP′ $< -1\sigma$) and at 2-days lead and lag (Fig. 7). At 0 lag (middle panel), a low pressure system is centered slightly north of the basepoint and is flanked by highs with small positive values. (The decrease in the magnitude of SLP′ away from the basepoint is primarily due to a decorrelation of atmospheric fields in both space and time and does not necessarily indicate a decrease in the strength of highs and lows.) Broad bands of flux anomalies that have a positive tilt with latitude pass near the axis of the three pressure anomalies. The strongest upward heat flux anomalies are found about 20° west of the central low pressure. Relatively strong downward flux anomalies ($Q'_{sh} + Q'_{lh} < -30$ W m^{-2}) are located

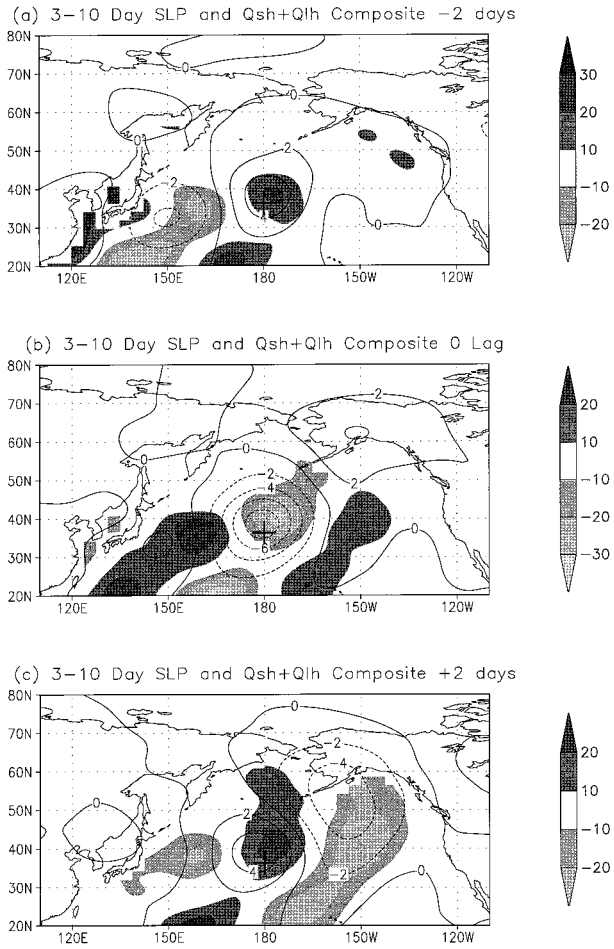

FIG. 7. Composites of 3–10-day filtered SLP′ (mb) and $Q'_{sh} + Q'_{lh}$ (W m^{-2}) over the North Pacific at (a) 2 days prior, (b) on the reference day (0 lag), and (c) 2 days after the SLP′ at the basepoint (+), located at 37°N, 180°, is less than -1σ (-6.0 mb). The composites consist of 207 cases. SLP′ are contoured at 2-mb intervals with negative contours dashed, while the $Q'_{sh} + Q'_{lh}$ is shaded at 10 W m^{-2} intervals where positive (negative) anomalies get darker (lighter) with increasing magnitude.

just northeast of the central low and more than 2000 km southwest of the storm center. These dual centers are due in part to differences in Q_{sh} and Q_{lh} anomalies: the magnitude of Q'_{sh} reaches a maximum at ~40°N while Q'_{lh} is maximized at ~20°N, resulting in a relative minimum in $|Q'_{sh} + Q'_{lh}|$ at around 30°N. In addition, $Q_{sh} + Q'_{lh}$ due to wind speed anomalies and those due to temperature plus moisture anomalies tend to cancel each other just to the south of the low (see section 3c and Fig. 14), which also contributes to the gap in the downward flux anomalies near 30°N and the date line.

The heat flux anomalies are consistent with the circulation around the low, upward flux anomalies are associated with northerly winds and the advection of cold dry air behind the low, with the reverse occurring ahead of the low. The negative $Q_{sh} + Q_{lh}$ anomaly centered at 22°N, 165°E (Fig. 7b) is located just east of a slight kink in the surface pressure field that extends southwest from the low. Analysis of the 1000–500-mb thickness anomalies (not shown) suggests that this kink in the SLP field is a cold front with negative (positive) heat flux anomalies occurring within the warm (cold) sector ahead of (behind) the front.

Figures 7a and 7c indicate the change in the position and strength of the SLP and flux anomalies at −2- and +2-days lag, two days before and after the low passes near the basepoint. From a lag of −2 days to 0 lag, the low pressure center tracks eastward from east of Japan to the center of the basin; it then tracks northeastward approaching southern Alaska 2 days later. In the central and west part of the basin the SLP anomalies are nearly concentric. In the eastern part of the basin the climatological flow is diffluent, which acts to strain synoptic eddies, causing the SLP anomalies to elongate meridionally or split the storm track in two (Whitaker and Dole 1995). In this region, southerly wind anomalies advect warm moist air ahead of either the one long cold front or in the warm sector of storms traveling along a north or south track; either case results in downward heat flux anomalies that extend all the way from Alaska to the southern edge of the basin.

Composites of SLP′ and $Q'_{sh} + Q'_{lh}$ in the 3–10-day band over the Atlantic at −2-, 0-, and +2-days lag (Fig. 8) are based on the 220 cases when the SLP at 0 lag is less than -1σ (-8.1 mb) at 52°N, 35°W. As in the Pacific, at 0 lag a strong low is flanked by highs with positive (negative) heat flux anomalies to the southwest (northeast) of the low. The SLP anomalies also propagate northeastward, crossing the basin in ~6 days. In contrast to the Pacific, the flux anomalies are zonally elongated and strong downward heat flux anomalies do not occur ahead of the cold front south of the low's center. In addition, while the low is ~25% stronger in the Atlantic than in the Pacific at 0 lag, its magnitude 2 days later is ~30% smaller compared with its Pacific counterpart, suggesting that storms are either more variable and/or decay more rapidly in the Atlantic.

The analyses of SLP and $Q_{sh} + Q_{lh}$ on synoptic timescales suggests that the GCM is reproducing many of the observed features of marine midlatitude cyclones, though some differences can be noted as well. The SLP and $Q_{sh} + Q_{lh}$ from the model resemble observations of midlatitude storms in terms of their shape and structure, though they tend to be of larger scale and somewhat weaker than typical storms in the real world. Several factors contribute to a broader scale: (i) the model's resolution is too coarse to represent strong fronts and tight SLP gradients, (ii) composites smooth out and enlarge the features, and (iii) filtering on 3–10 days extracts the larger scale component of the synoptic variability; when the data were filtered retaining periods of 2–6 days (a la Blackmon et al. 1977), the zonal extent of the individual cyclones decreased by about one-third. In addition, the track and strength of surface highs and lows in Figs. 7 and 8 are influenced by the criteria used

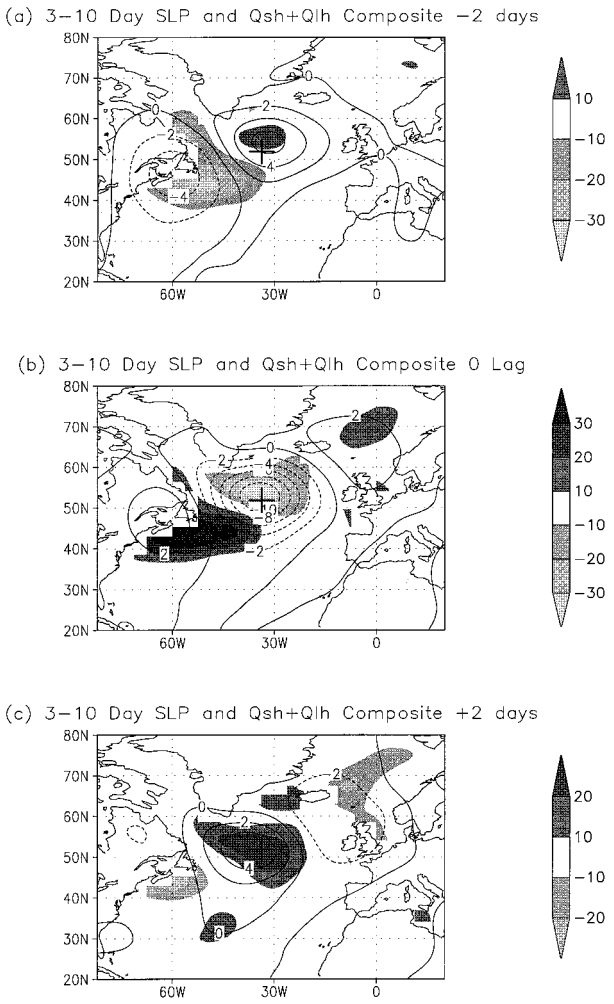

FIG. 8. Composites of 3–10-day filtered SLP′ (mb) and $Q'_{sh} + Q'_{lh}$ (W m^{-2}) over the North Atlantic at (a) 2 days prior, (b) on the reference day, and (c) 2 days after the SLP′ at the basepoint, located at 52°N, 35°W, is less than -1σ (-8.1 mb). The composites consist of 220 cases; contour interval and shading as in Fig. 7.

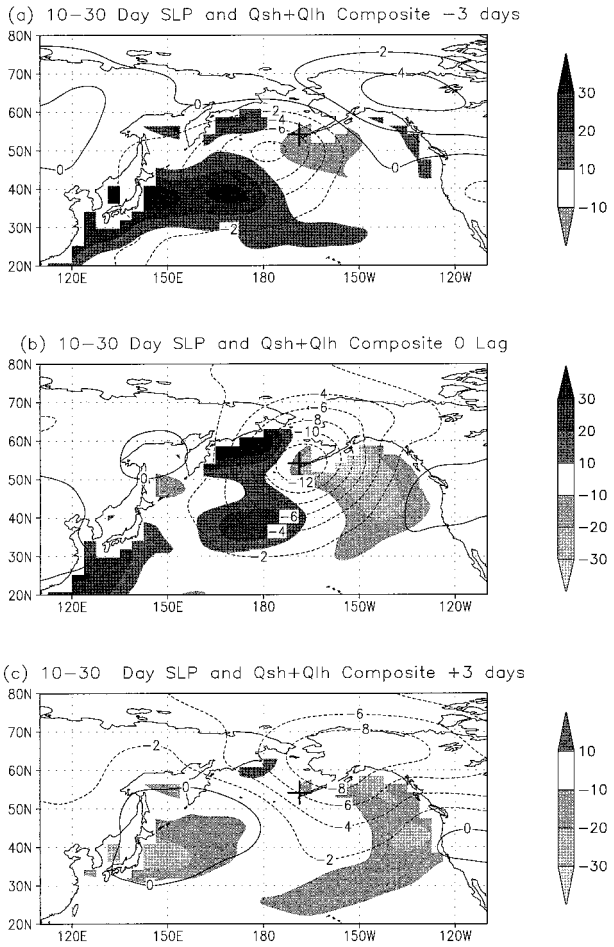

FIG. 9. Composites of 10–30-day filtered SLP′ (mb) and $Q'_{sh} + Q'_{lh}$ (W m^{-2}) over the North Pacific at (a) 3 days prior, (b) on the day, and (c) 3 days after the SLP′ at the basepoint, located at 54°N, 170°W, is less than -1σ (-10.0 mb). The composites consist of 262 cases; contour interval and shading as in Fig. 7.

to composite the model fields. Composites of SLP′ and $Q'_{sh} + Q'_{lh}$, based on a $+1\sigma$ SLP criteria (not shown), obtain anomalies of similar magnitude and shape but of opposite sign to the -1σ SLP composite, suggesting a linear relationship between SLP and the surface fluxes.

The results of the composite analyses also depend on the position of the basepoint. The basepoint in the Pacific is located 10°–15° south of the center of the storm track but in a region of large $Q_{sh} + Q_{lh}$ variability in the 3–10-day band as indicated by Fig. 4a. This results in the maximum SLP′ to be located slightly north of the basepoint but still obtains relatively strong storms that are associated with the dominant pattern of surface flux anomalies, as can be seen by comparing $Q'_{sh} + Q'_{lh}$ composites (Fig. 7) and EOFs (Fig. 5). In addition, the evolution of storms remains over the ocean for the three composite periods. The basepoint in the Atlantic is within the dominant storm track and the flux anomalies from the composite and EOF analyses are similar as well. Moving the basepoint in either basin does not affect the general structure of the SLP′ and $Q'_{sh} + Q'_{lh}$ fields but does change the magnitude of the anomalies (not shown). For example, moving the Atlantic basepoint from 52°N, its present location, to 37°N, the same latitude as the Pacific basepoint, decreases the magnitude of both SLP′ and $Q'_{sh} + Q'_{lh}$ by roughly 50%.

Composites of 10–30-day filtered SLP′ and $Q'_{sh} + Q'_{lh}$ at lags of -3, 0, and $+3$ days over the North Pacific and North Atlantic Oceans are shown in Figs. 9 and 10, respectively. While the magnitude of the SLP anomalies in the lower-frequency band are similar to those in the synoptic band, their scale is much broader and they progress more slowly eastward, consistent with the observed space–time frequency spectra and observations of propagating Rossby waves and cutoff lows (Blackmon et al. 1984; Kushnir and Wallace 1989; Dole and

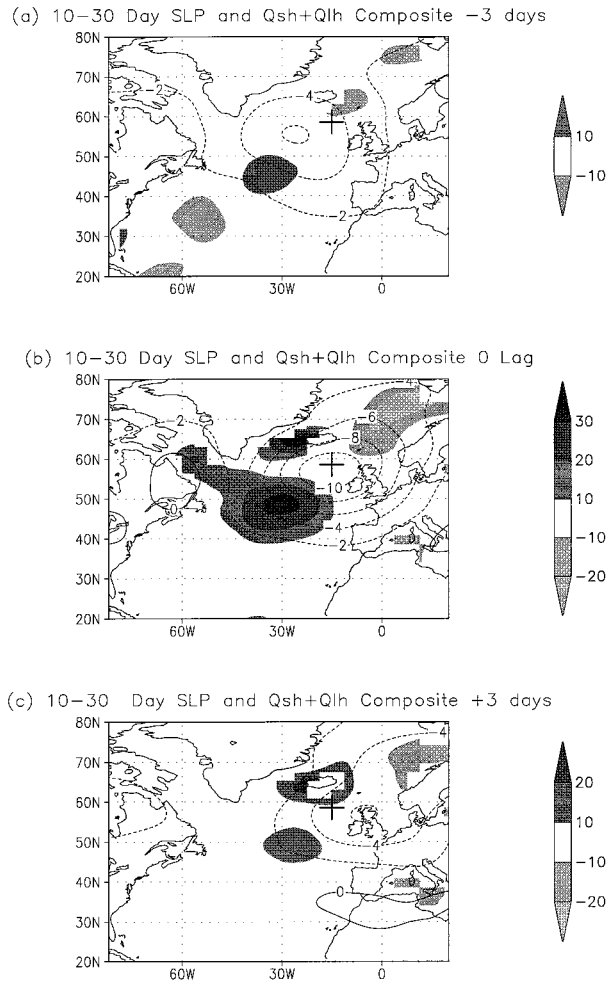

FIG. 10. Composites of 10–30-day filtered SLP′ (mb) and $Q'_{sh} + Q'_{lh}$ (W m^{-2}) over the North Atlantic at (a) 3 days prior, (b) on the day, and (c) 3 days after the SLP′ at the basepoint, located at 58°N, 15°30′W, is less than -1σ (-7.3 mb). The composites consist of 254 cases; contour interval and shading as in Fig. 7.

Black 1990). In both the Pacific and Atlantic, two positive $Q_{sh} + Q'_{lh}$ centers are located about ~20° west of the low at 0 lag (Figs. 9b and 10b). The northern center is near the Siberian Peninsula in the Pacific, and Greenland in the Atlantic, so the anomalous cyclonic circulation can advect cold dry air over the adjoining ocean, creating large upward heat flux anomalies. The southern center located far from land and at the terminus of the northerly winds appears to be more directly related to the anomalous circulation. A negative $Q'_{sh} + Q'_{lh}$ center is found to the east of the low in the Pacific but to the northeast of the low in the Atlantic; this difference is likely shaped by the geometry of the basins, since open water is found to the northeast of the basepoint only in the Atlantic. The anomaly patterns obtained from the composite analyses at 0 lag resemble the leading EOF of 10–30-day filtered $Q'_{sh} + Q'_{lh}$ (not shown) over the North Pacific and Atlantic Oceans.

c. *Dependence of the flux anomalies on the atmosphere–ocean variables*

To examine the relative influence of the air-sea temperature difference and the wind speed on the sensible heat flux anomalies, we first expand the variables in (1) into their mean and anomalous components:

$$Q'_{sh} = \rho c_H c_p [\overline{U}\,\Delta T' + U'\overline{\Delta T} + (U'\Delta T' - \overline{U'\Delta T'})], \quad (3)$$

where $\bar{(\,)}$ indicates a long-term monthly mean for one of the winter months, $(')$ the daily departure from that mean, and $\Delta T = \text{SST} - T_{air}$. The full value of ρ ($\overline{\rho} + \rho'$) is used in (3); however, air density anomalies contribute little to Q'_{sh} as $\rho' \ll \overline{\rho}$. Recall from section 2 that c_H (and c_e) are constants and that the SSTs repeat the same seasonal cycle each year in this model simulation. Thus, $c'_H = 0$, and $\Delta T'$ is given by T'_{air}. As discussed in section 2, the archived values of Q_{sh} differ from those computed off-line using (1) or (3) because (i) Q_{sh} is stored as a daily average, while T_{air} and U are stored as instantaneous values, and (ii) T_{air} and U used to compute Q_{sh} are modified by additional processes before being archived. In this section we have calculated Q'_{sh}, using the archived values of U, and T_{air}, in order for Q'_{sh} to equal the sum of the terms on the right hand side of (3).

During DJF, the daily values of the three terms on the right hand side of (3) are regressed separately on Q'_{sh} at each model grid point, indicating the local fraction of Q'_{sh} related to thermal anomalies ($\overline{U}\Delta T'$), wind speed anomalies ($U'\overline{\Delta T}$), and the covariance between the two ($U'\Delta T' - \overline{U'\Delta T'}$). The regression values of $\overline{U}\Delta T'$ and $U'\overline{\Delta T}$ (multiplied by $\rho c_H c_p$) are presented in Fig. 11 for the North Pacific and Atlantic Oceans; the covariance term (not shown) has a small contribution with values of less than 0.2 over almost all of the domain. In the Pacific, more than half of Q'_{sh} can be attributed to $\overline{U}\Delta T'$ along much of the west coast of North America and within a band extending from the South China Sea to the Gulf of Alaska. In the Atlantic, $\overline{U}\Delta T'$ is the dominant term over most of the basin north of 35°N. Here, Q'_{sh} is dominated by $U'\overline{\Delta T}$ (Fig. 11b) in the northwest Pacific and in the central part of both oceans south of 25°N.

The contribution of wind speed and moisture to the latent heat flux anomalies are analyzed by decomposing these variables in (2) into their mean and anomalous parts:

$$Q'_{lh} = \rho c_e L [\overline{U}\,\Delta q' + (U'\overline{\Delta q} + (U'\Delta q' - \overline{U'\Delta q'})], \quad (4)$$

where $\Delta q = q_{sat} - q_{air}$ and the archived values of U and q_{air} have been used to calculate Q'_{lh}. The local regression values of $\overline{U}\Delta q'$ and $U'\overline{\Delta q}$, multiplied by $\rho c_e L$ on Q'_{lh}, are shown in Fig. 12; as with Q'_{sh}, the covariance term ($U'\Delta q' - \overline{U'\Delta q'}$) is not shown since its contribution to Q'_{lh} is much smaller than the other two terms. The general pattern of both $\overline{U}\Delta q'$ and $U'\overline{\Delta q}$ are similar to their

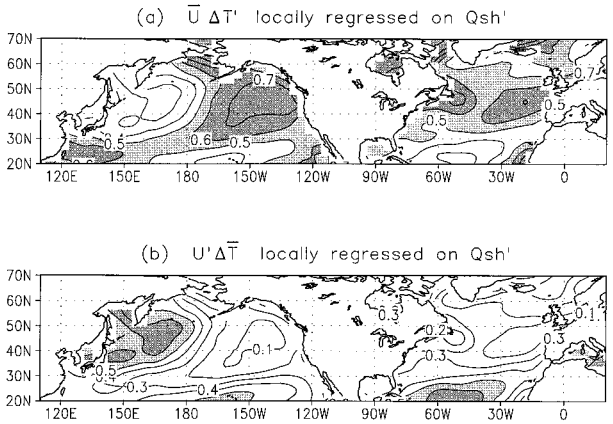

FIG. 11. Local regression values of $\rho c_H c_p$ times (a) $\overline{U}\Delta T'$ and (b) $U'\overline{\Delta T}$ on Q'_{sh}. The unitless values represent the fraction of Q'_{sh} related to the thermal and wind speed anomalies at that grid point. Contour interval is 0.1 and values between 0.5–0.6 are shaded light, while those greater than 0.6 are shaded dark.

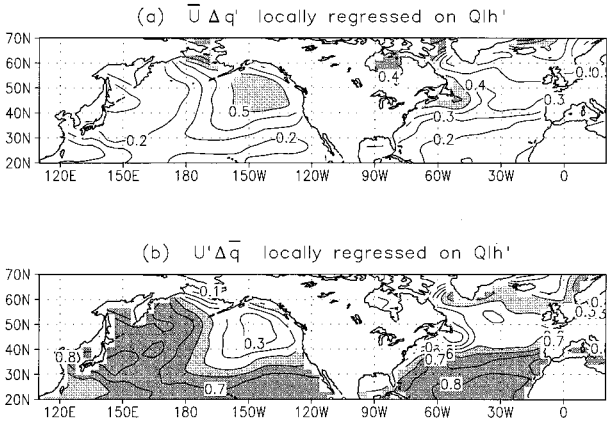

FIG. 12. Local regression values of $\rho c_e L$ times (a) $\overline{U}\Delta q'$ and (b) $U'\overline{\Delta q}$ on Q'_{lh}. The unitless values represent the fraction of Q'_{lh} related to (a) moisture and (b) wind speed anomalies at that grid point. Contour interval and shading as in Fig. 11.

sensible heat flux counterparts. However, the term related to U' has a much greater impact on controlling the latent than the sensible heat flux anomalies, since $\overline{\Delta q}/q' > \overline{\Delta T}/T'$. As a result, the fraction of Q'_{lh} associated with $U'\overline{\Delta q}$ exceeds 0.5 over all but the northeast quadrant in the Pacific Ocean and south of 40°N in the Atlantic, and it exceeds 0.7 over most of the subtropics in both basins. Since warmer air has a higher saturation mixing ratio, $\overline{\Delta q}$ is 3 to 5 times larger over the subtropical oceans compared with high latitudes, resulting in a greater Q'_{lh} in the subtropics per unit change in U' (Cayan 1992).

Following Klein et al. (1995), ''standard anomalies'' of Q'_{sh} associated with $\overline{U}\Delta T'$ and with $U'\overline{\Delta T}$ are defined by the product of the regression values shown in Fig. 11a,b with a $+ 1\sigma$ change in Q'_{sh} at each grid point. Standard anomalies of $\overline{U}\Delta q'$ and $U'\overline{\Delta q}$ are computed in a similar fashion. The standard anomalies of $\overline{U}\Delta T'$ and $\overline{U}\Delta q'$ are then added together, as are $U'\overline{\Delta T}$ and $U'\overline{\Delta q}$, to represent a typical anomaly in $Q'_{sh} + Q'_{lh}$ associated with the mean and anomalous wind speed, respectively. While the standard anomalies associated with Q_{sh} and Q_{lh} are computed independently and then summed together, the two are highly correlated because the amount of moisture in the atmosphere over the ocean boundary layer is highly dependent on the temperature (e.g., Battisti et al 1995; Alexander and Penland 1996). The standard anomalies of $\overline{U}\Delta T' + \overline{U}\Delta q'$ exceed 45 W m^{-2} in the South China Sea, Bering Sea, and the northeast Pacific (Fig. 13a), while $U'\overline{\Delta T} + U'\overline{\Delta q}$ (Fig. 13b) exceeds 45 W m^{-2} in the subtropics and 90 W m^{-2} to the east of Japan. In the latter region, $\overline{\Delta T}$ and $\overline{\Delta q}$ are large as cold dry air advected off the continents overrides warm water associated with the Kuroshio current. A similar phenomena appears to occur in the Atlantic over the Gulf stream, but the flux anomaly associated with $U'\overline{\Delta T} + U'\overline{\Delta q}$ is smaller in scale and magnitude.

In the Pacific, the pattern of $\overline{U}\Delta T'$ and $\overline{U}\Delta q'$ (Figs. 11a–13a) closely resembles that of the standard deviation of the anomalous meridional wind (σ of v′; Alexander and Scott 1996a), as v′ operating on the strong mean meridional gradients of air temperature and humidity creates anomalies in T_{air} and q_{air}, and thus Q_{sh} and Q_{lh}. Using regression and correlation analyses, Cayan (1992) and Alexander and Scott (1996b) found a strong relationship between v′ and $Q'_{sh} + Q'_{lh}$ over the northern oceans. Like $\overline{U}\Delta T'$ and $\overline{U}\Delta q'$, σ of v′ is relatively large over the Bering Sea and in a band that widens as it extends from south of Japan to west of Vancouver Island. Circulation anomalies on both inter-

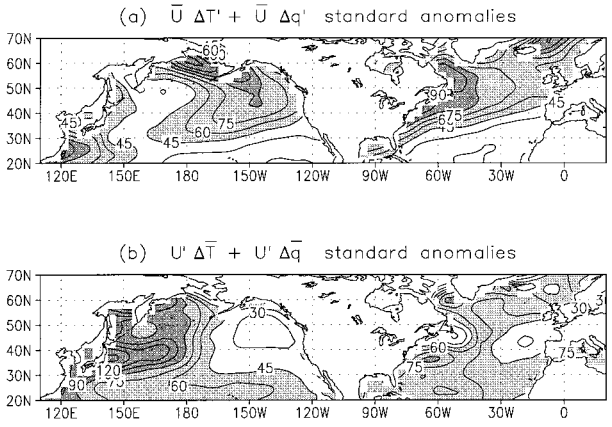

FIG. 13. Standard anomalies of (a)$\overline{U}(\Delta T' + \Delta q')$ and (b) $U'(\overline{\Delta T} + \overline{\Delta q})$, where ΔT and Δq have been multiplied by $\rho c_H c_p$ and $\rho c_e L$, respectively, to obtain units of W m^{-2}. The standard anomalies represent typical $Q'_{sh} + Q'_{lh}$ values associated with the (a) mean and (b) anomalous wind speed at that grid point. Contour interval is 15 W m^{-2} and values between 45–90 are shaded light, while those greater than 90 are shaded dark.

annual and intraseasonal timescales contribute to $\overline{U}\Delta T' + \overline{U}\Delta q'$ via v′. On interannual timescales, the SLP′ pattern (Fig. 1) indicates that |v′| is large over the north and eastern parts of the basin when the Aleutian low is stronger or weaker than normal. On submonthly timescales, v′ in the vicinity of cold fronts creates flux anomalies especially in the northeast Pacific (Figs. 5, 7c, and 9b,c). While v′ also contributes to $Q_{sh} + Q'_{lh}$ through $U'\overline{\Delta T} + U'\overline{\Delta q}$, the relatively small mean air-sea temperature and moisture difference plus strong mean winds lead it to be more closely associated with $\overline{U}\Delta T'$ and $\overline{U}\Delta q'$ in the northeast Pacific.

The contribution of wind speed anomalies to the surface flux anomalies is strikingly different in the northwest Pacific, where $U'\overline{\Delta T}$ and $U'\overline{\Delta q}$ have a significant contribution to Q'_{sh} and Q'_{lh}, compared with the northwest Atlantic, where these terms have a negligible contribution to the flux anomalies (Figs. 11–13). In general, $\overline{\Delta T}\,(\overline{\mathrm{SST}} - \overline{T_{air}}) > 5°\mathrm{C}$ on the western side of the northern oceans. However, the Labrador Current transports very cold water south along the east coast of Canada resulting in cold SSTs and, thus, $\overline{\Delta T}$ and $\overline{\Delta q}$ are relatively small in the northwest Atlantic. In contrast, there is little flow through the Bering Strait into the Pacific. In addition, the air over Asia is colder than over North America during winter; the advection of this air out over the oceans by the mean westerlies also contributes to larger $\overline{\Delta T}$ and $\overline{\Delta q}$ in the northwest Pacific compared with the Atlantic.

The three components of $Q_{sh} + Q'_{lh}$ on synoptic timescales are examined by first time filtering the data retaining periods of 3–10 days and then compositing each component separately based on when the SLP′ $< -1\sigma$ at the same Pacific and Atlantic grid points used in section 3b. The components are given by $\overline{U}(\Delta T' + \Delta q')$, $U'(\overline{\Delta T} + \overline{\Delta q})$, and $U'(\Delta T' + \Delta q') - \overline{U'(\Delta T' + \Delta q')}$, where ΔT and Δq have been multiplied by $\rho c_H c_p$ and $\rho c_e L$, respectively, to obtain units of W m^{-2}. In the Pacific (Fig. 14), the pattern of $\overline{U}(\Delta T' + \Delta q')$ resembles that of $Q'_{sh} + Q'_{lh}$, with negative anomalies ahead of the low (see Fig. 7b) and positive anomalies behind it, and the anomaly centers have a southwest to northeast tilt. This structure is related to the direction of wind anomalies on either side of the cold front, which extends southwest from the low; east of the front, southerlies advect warm moist air over cold water, resulting in $\Delta T'$ and $\Delta q' < 0$, while the reverse occurs about 1000–2000 km west of the front. In contrast, $U'(\overline{\Delta T} + \overline{\Delta q})$ reaches a maximum just to the south of the low and has a zonal orientation. Strong SLP gradients in the vicinity of the low lead to strong wind anomalies, especially to the south of the low where the cyclonic circulation acts to enhance the mean westerlies. Near 170°E in the subtropical Pacific, the westerly wind anomalies oppose the mean trade winds, resulting in a decrease in the wind speed and, thus, $U'(\overline{\Delta T} + \overline{\Delta q}) < 0$. $U'(\overline{\Delta T} + \overline{\Delta q})$ and $\overline{U}(\Delta T' + \Delta q')$ have similar magnitudes that reach 70 W m^{-2} and tend to cancel each other near the low's center but reinforce each other at the very southern edge of the cyclonic circulation. The two terms have similar patterns and signs relative to the basepoint, regardless of where the basepoint is located; however, $\overline{U}(\Delta T' + \Delta q')$ dominates when the basepoint is located in the far western part of the ocean basins (not shown). On synoptic timescales, the covariance term is about one-third to one-fifth as large as the other two and acts to reinforce $\overline{U}(\Delta T' + \Delta q')$ by enhancing the downward (upward) heat fluxes east (west) of the storm. The relationship between the three components is similar in the Atlantic (Fig. 15) in that the $\overline{U}$ and covariance terms indicate that the flux anomalies are negative ahead of the low (see Fig. 8b) and positive behind it, while the U′ term has positive flux anomalies centered just to the south of the low.

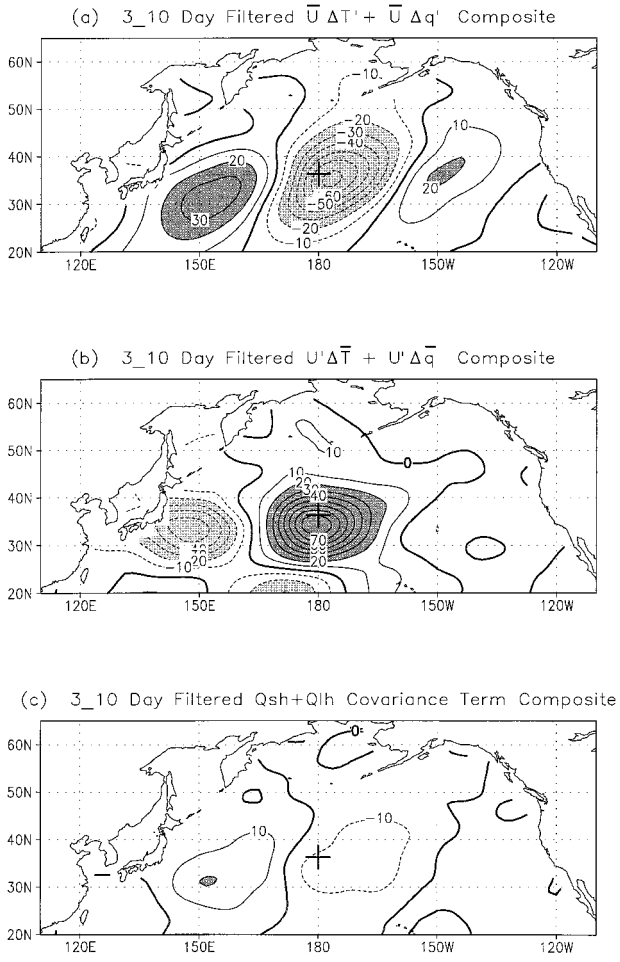

FIG. 14. Composites of the 3–10-day filtered components of $Q'_{sh} + Q'_{lh}$ over the North Pacific: (a) $\overline{U}(\Delta T' + \Delta q')$; (b) $U'(\overline{\Delta T} + \overline{\Delta q})$; and (c) the covariance term $U'(\Delta T' + \Delta q') - \overline{U'(\Delta T' + \Delta q')}$, where ΔT and Δq have been multiplied by $\rho c_H c_p$ and $\rho c_e L$, respectively. The composites are constructed as in Fig. 7b, when SLP′ at the basepoint is less than -1σ. The contour interval is 10 W m^{-2}, where negative anomalies are dashed and anomalies greater than than 20 W m^{-2} are shaded dark, while those less than -20 W m^{-2} are shaded light.

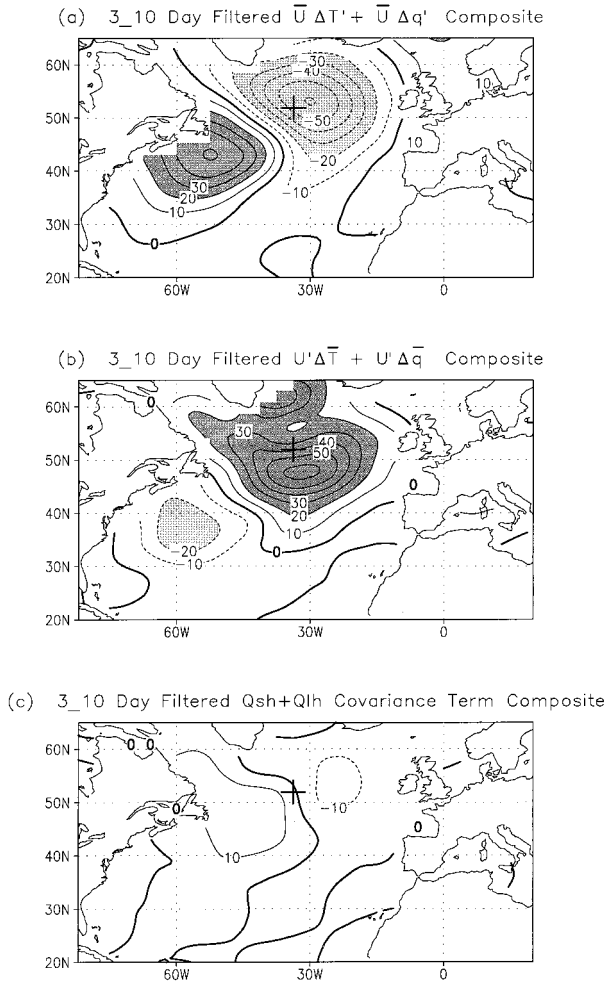

FIG. 15. Composites of the 3–10-day filtered components of $Q'_{sh} + Q'_{lh}$ over the North Atlantic: (a) $\overline{U}(\Delta T' + \Delta q')$; (b) $U'(\overline{\Delta T}$ plus; $\overline{\Delta q})$; and (c) the covariance term $U'(\Delta T' + \Delta q') - \overline{U'(\Delta T' + \Delta q')}$, where ΔT and Δq have been multiplied by $\rho c_H c_p$ and $\rho c_e L$, respectively. The composites are constructed as in Fig. 8b, when SLP′ at the basepoint is less than -1σ. Contour interval and shading as in Fig. 14.

4. Summary and conclusions

Daily fields obtained from a 17-yr GFDL atmospheric GCM simulation are used to study surface sensible (Q_{sh}) and latent (Q_{lh}) heat flux variability and their relationship to the near-surface atmospheric circulation as indicated by the SLP field. The model fluxes, computed using bulk aerodynamic formula, depend on the wind speed and the air–sea temperature and humidity difference. The ocean boundary conditions repeat the same climatological seasonal cycle each year, so Q_{sh} and Q_{lh}, the dominant midlatitude surface fluxes in winter, are not influenced by SST variability. We focus on the interannual and intraseasonal variability of Q_{sh} and Q_{lh} over the North Pacific and North Atlantic Oceans in winter (December–February). The intraseasonal variability is examined further by filtering the model fields retaining periods of 3–10 and 10–30 days.

The EOF analyses indicate that the leading mode of SLP interannual variability over the northern oceans are basin-wide features that consist of a single center associated with the strength and position of the Aleutian low in the Pacific, and a dipole pattern associated with the Icelandic low and Azores high in the Atlantic. The large-scale surface flux anomaly patterns are clearly organized by the low-level atmospheric circulation associated with the dominant SLP modes in agreement with the observational studies of Cayan (1992a,b) and Iwasaka and Wallace (1995).

Surface flux variability on all of the timescales examined is maximized along the north and west edges of both oceans and between Japan and the dateline at ~35°N in the Pacific. The pattern of interannual standard deviation of $Q_{sh} + Q_{lh}$ in the GCM resemble observations (Zhao and McBean 1986; Cayan 1992a), but the magnitude of the simulated anomalies are ~20% smaller. The intraseasonal variability in the model is approximately 3–5 times larger than the interannual variability in agreement with Cayan's (1992) observational analysis. More than half of the total surface flux variability in winter over most of the North Hemisphere Oceans occurs on timescales of less than 30 days, with fluctuations in the 3–10-day band contributing slightly more to the variance than those in 10–30-day band north of the subtropics.

Surface flux variability in the 3–10-day time band is clearly associated with midlatitude storms. Alternating bands of positive (upward) and negative (downward) surface flux anomalies are associated with a series of high and low pressure systems over the oceans, with maximum amplitudes on the west side of both ocean basins. Like disturbances in the 3–10-day band, those in the 10–30-day band have strong and coherent SLP anomaly centers that propagate eastward, where positive (negative) $Q_{sh} + Q_{lh}$ anomalies are located west (east) of the low's center with magnitudes exceeding 30 W m^{-2}. However, the anomalies in the 10–30-day band are centered farther north, are broader in scale, and propagate ~3–4 times slower than the synoptic disturbances. These features bear some resemblance to the slow-moving large-scale cutoff lows described by Dole and Black (1990) and Black and Dole (1993). They may also reflect propagating Rossby waves, blocking events, and changes in the preferred storm tracks.

The sensible and latent heat flux are proportional to the product of the wind speed (U) with the ocean–atmosphere temperature (ΔT) and humidity (Δq) difference, respectively. Thus, surface flux anomalies depend on both mean ($\bar{}$) and anomalous ($'$) conditions. Here, $\overline{U}(\Delta T' + \Delta q')$ is the dominant contributor to $Q_{sh} + Q'_{lh}$ over the northeast Pacific and much of the Atlantic north of 40°N, while $U'(\overline{\Delta T} + \overline{\Delta q})$ dominates in the subtropics, in agreement with Halliwell

and Mayer (1996), and in the western Pacific. The contribution to Q'_{sh} and Q'_{lh} due to the covariance between U' and $\Delta T'$ or $\Delta q'$ is generally smaller than the other two terms. Cayan (1992) found that the flux anomalies have a greater dependence on $\Delta T'$ and $\Delta q'$ that in our study. Several factors may account for this disparity including: our calculations are performed with daily rather than monthly anomalies; differences between the GFDL GCM and observations; and the absence of SST anomalies in our analysis.

Overall, the relationship between the anomalous atmospheric circulation and surface fluxes are similar in the North Atlantic and Pacific Oceans on the intraseasonal and interannual timescales examined here. Both are dominated by large-scale circulation patterns on interannual timescales, although the leading pattern is a monopole in the Pacific and dipole in the Atlantic. However, the storm track and associated surface flux anomalies are located farther north and their axis has a greater southwest–northeast tilt in the Atlantic compared with the Pacific. The fluxes in the two basins are also influenced by the ocean circulation via its impact on the mean SST field and by the land–sea distribution. Cold water supplied to the northwest Atlantic by the Labrador Current has no counterpart in the Pacific. In addition, the continental air, which is subsequently advected eastward over the oceans, is colder over Asia than North America. Both of these processes result in small $\overline{\Delta T}$ and $\overline{\Delta q}$ values at ~45°N in the west Atlantic relative to the west Pacific, and thus $Q'_{sh} + Q'_{lh}$ east of Newfoundland primarily result from anomalies in air temperature and humidity since $U'(\overline{\Delta T} + \overline{\Delta q})$ is small.

The distribution and magnitude of the surface heat flux anomalies on subseasonal timescales can influence the development of SST anomalies, mixed layer depth, and the buoyancy driven circulation. The ocean surface is cooled in the wake of midlatitude cyclones directly by the sensible and latent heat fluxes, and indirectly by entraining cold water into the surface mixed layer via enhanced oceanic convection and mechanical mixing. Much of the normal cooling that occurs in fall and the formation of seasonal SST anomalies may result from the passage of a few strong storms. Miyakoda and Rosati (1984), Polonsky et el. (1992) and Kraus and Businger (1994) examine mechanisms by which surface flux variability on submonthly timescales can influence low-frequency fluctuations in the ocean. Large surface flux anomalies associated with storms in the Labrador and Greenland Seas (Figs. 6 and 8) are believed to play an important role in deep water formation (Clarke and Gascard 1983; Killworth 1983).

The results from this study suggest that the leading patterns of surface flux variability on interannual or shorter timescales do not depend on either local or remote SST anomalies, since the SST boundary conditions repeat the same seasonal cycle each year of the GCM simulation. However, the inclusion of an interactive ocean could influence the magnitude of the fluxes or have subtle effects on the atmospheric circulation. Recent studies by Barsugli (1995), Blade (1997), and Bhatt et al. (1997) indicate that the patterns of midlatitude atmospheric variability are nearly unchanged in coupled atmosphere–ocean models, but the near-surface air temperature variability is enhanced while the surface flux variability is reduced relative to prescribed SST runs. In coupled runs, the SST and air temperature come into equilibrium resulting in smaller values of $\Delta T'$ and $\Delta q'$, thus reducing $Q'_{sh} + Q'_{lh}$ especially at periods longer than a season. However, SST anomalies resulting from oceanic advection, not included in the model studies cited above, could enhance flux variability (Luksch 1996). In addition, midlatitude surface flux variability is enhanced by the atmospheric response to remote SST anomalies, such as those associated with El Niño events (Alexander 1990, 1992; Lau and Nath 1996).

Studies by Lanzante (1983), Palmer and Sun (1985), and Ting and Peng (1995) suggest that SST anomalies influence midlatitude storm tracks, which in turn affects the jet stream and stationary wave patterns. While the influence of SST anomalies is communicated to the atmosphere via the surface heat fluxes, possibly by preconditioning the atmospheric environment to storm development (Nuss 1989; Kuo et al. 1991), the detailed mechanism of this transfer process remains an open question. In future work, we plan to study the development of storms in response to SST anomalies using GCM simulations and the 4-times daily NCEP Re-analysis.

Acknowledgments. The model fields were provided by Isaac Held, Gabriel Lau, and Peter Phillips as part of the GFDL-University Consortium project. We thank Joe Barsugli, Clara Deser, Jeff Whitaker, and two anonymous reviewers for their valuable suggestions. This research was supported by a grant from the NOAA Office of Global Programs.

REFERENCES

Alexander, M. A., 1990: Simulation of the response of the North Pacific Ocean to the anomalous atmospheric circulation associated with El Niño. *Climate Dyn.,* **5,** 53–65.

——, 1992: Midlatitude atmosphere–ocean interaction during El Niño. Part I: The North Pacific Ocean. *J. Climate,* **5,** 944–958.

——, and J. D. Scott, 1995: Atlas of climatology and variability in the GFDL R30S14 GCM. CIRES, University of Colorado, U.S. Goverment Printing Office 1996-774-842, 121 pp. [Available from University of Colorado, CIRES, Box 449, Boulder, CO 80309.]

——, and C. Penland, 1996: Variability in a mixed layer model of the upper ocean driven by stochastic atmospheric surface fluxes. *J. Climate,* **9,** 2424–2442.

——, and J. D. Scott, 1996a: Web-based atlas of climatology and variability in the GFDL R30S14 GCM. [Available on-line from http://www.cdc.noaa.gov/gfdl.]

——, and ——, 1996b: Surface flux variability over the North Pacific in a GCM. *Proc. Twentieth Annual Climate Diagnostic Workshop,* Seattle, WA, National Oceanographic and Atmospheric Administration, 222–225.

Barsugli, J. J., 1995: Idealized models of intrinsic midlatitude atmosphere-ocean interaction. Ph.D. dissertation, University of Washington, 187 pp. [Available on-line from http://www.cdc.noaa.gov/~jjb/thesis.html.]

Battisti, D. S., U. S. Bhatt, and M. A. Alexander, 1995: A modeling study of the interannual variability in the wintertime North Atlantic Ocean. *J. Climate,* **8,** 3067–3083.

Bhatt, U. S., M. A. Alexander, D. S. Battisti, D. D. Houghton, and L. M. Keller, 1997: Atmosphere–ocean interaction in the North Atlantic: Near-surface climate variability. *J. Climate,* in press.

Black, R. X., and R. M. Dole, 1993: The dynamics of large-scale cyclogenesis over the North Pacific Ocean. *J. Atmos. Sci.,* **50,** 421–442.

Blackmon, M. L., J. M. Wallace, N. C. Lau, and S. L. Mullen, 1977: An observational study of the Northern Hemisphere wintertime circulation. *J. Atmos. Sci.,* **34,** 1040–1053.

——, Y.-H. Lee, J. M. Wallace, and H.-H. Hsu, 1984: Time variation of 500-mb height fluctuations with long intermediate and short timescales as deduced from lag-correlation statistics. *J. Atmos. Sci.,* **41,** 981–991.

Blade, I., 1997: The influence of midlatitude ocean–atmosphere coupling on the low-frequency variability of a GCM. Part I: No tropical SST forcing. *J. Climate,* **10,** 2087–2106.

Bretherton, C. S., C. Smith, and J. M. Wallace, 1992: An intercomparison of methods for finding patterns in climate data. *J. Climate,* **5,** 541–560.

Camp, N. T., and R. L. Elsberry, 1978: Oceanic thermal response to strong atmospheric forcing II. The role of one-dimensional processes. *J. Phys. Oceanogr.,* **8,** 215–224.

Cayan, D. R., 1992: Variability of latent and sensible heat fluxes estimated using bulk formulae. *Atmos.–Ocean,* **30,** 1–42.

Elsberry, L. E., and N. T. Camp, 1978: Oceanic thermal response to strong atmospheric forcing I. Characteristics of forcing events. *J. Phys. Oceanogr.,* **8,** 206–214.

Frankignoul, C., and K. Hasselmann, 1977: Stochastic climate models. Part 2. Application to sea-surface temperature variability and thermocline variability. *Tellus,* **29,** 284–305.

——, and R. W. Reynolds, 1983: Testing a dynamical model for midlatitude sea surface temperature anomalies. *J. Phys. Oceanogr.,* **13,** 1131–1145.

Gordon, C. T., and W. Stern, 1982: A description of the GFDL global spectral model. *Mon. Wea. Rev.,* **110,** 625–644.

Gulev, S. K., 1997: Climate variability of the intensity of synoptic processes in the North Atlantic midlatitudes. *J. Climate,* **10,** 574–592.

Hall, A., and S. Manabe, 1996: Can local linear stochastic theory explain sea surface temperature and salinity variability. *Climate Dyn.,* **13,** 167–180.

Halliwell, G. R., 1997: Simulation of North Atlantic decadal/multidecadal winter SST anomalies driven by basin-scale atmospheric circulation anomalies. *J. Phys. Oceanogr.,* in press.

——, and D. A. Mayer, 1996: Frequency response properties of forced climatic SST anomaly variability in the North Atlantic. *J. Climate,* **9,** 3575–3587.

Iwasaka, N., and J. M. Wallace, 1995: Large scale air sea interaction in the Northern Hemisphere from a view point of variations of surface heat flux by SVD analysis. *J. Meteor. Soc. Japan,* **73,** 781–794.

Killworth, P. D., 1983: Deep convection in the world ocean. *Rev. Geophys. Space Phys.,* **21,** 1–26.

Klein, S. A., D. L. Hartmann, and J. R. Norris, 1995: On the relationships among low-cloud structure, sea surface temperature, and atmospheric circulation in the summertime northeast Pacific. *J. Climate,* **8,** 1140–1155.

Kraus, E. B., and R. E. Morrison, 1966: Local interactions between sea and air at monthly and annual time scales. *Quart. J. Roy. Meteor. Soc.,* **92,** 114–127.

——, and J. A. Businger, 1994: *Atmosphere-Ocean Interaction.* 2d ed. *Oxford Monograms on Geology and Geophysics,* No. 27, Oxford University Press, 362 pp.

Kuo, Y.-H., and S. Lownam, 1990: Prediction of nine explosive cyclones over the western Atlantic Ocean with a regional model. *Mon. Wea. Rev.,* **118,** 3–25.

——, R. J. Reed, and S. Lownam, 1991: Effects of surface energy fluxes during the early development and rapid intensification stages of seven explosive cyclones in the western Atlantic. *Mon. Wea. Rev.,* **119,** 457–476.

Kushnir, Y., and J. M. Wallace, 1989: Low-frequency variability in the Northern Hemisphere winter: Geographical distribution, structure and time-scale dependence. *J. Atmos. Sci.,* **46,** 3122–3142.

Lanzante, J. R., 1983: A further assessment of the association between sea surface temperature gradient and the overlying midtropospheric circulation. *J. Phys. Oceangr.,* **13,** 1971–1974.

——, 1990: The leading modes of 10–30 day variability in the extratropics of the Northern Hemisphere during the cold season. *J. Atmos. Sci.,* **47,** 2115–2140.

Large, W. C., J. C. McWilliams, and S. C. Doney, 1994: Oceanic vertical mixing: A review and a model with a nonlocal boundary layer parameterization. *Rev. Geophys.,* **32,** 363–404.

Lau, N.-C., and M. J. Nath, 1996: The role of the ''atmospheric bridge'' in linking tropical Pacific ENSO events to extratropical SST anomalies. *J. Climate,* **9,** 2036–2057.

Luksch, U., 1996: Simulation of North Atlantic low-frequency variability. *J. Climate,* **9,** 2083–2092.

——, and H. von Storch, 1992: Modeling the low-frequency sea surface temperature variability in the North Pacific. *J. Climate,* **5,** 893–906.

Manabe, S., and D. G. Hahn, 1981: Simulation of atmospheric variability. *Mon. Wea. Rev.,* **109,** 2260–2286.

Miyakoda, K., and A. Rosati, 1984: The variation of sea surface temperature in 1976 and 1977. 2. The simulation with mixed layer models. *J. Geophys. Res.,* **89,** 6533–6542.

Monobianco, J., 1989: Explosive East Coast cyclogenesis over the west central North Atlantic Ocean: A composite study derived from ECMWF operational analyses. *Mon. Wea. Rev.,* **117,** 2365–2383.

Neiman, P., and M. A. Shapiro, 1993: The life cycle of an extratropical marine cyclone. Part I: Frontal-cyclone evolution and thermodynamic air–sea interaction. *Mon. Wea. Rev.,* **121,** 2153–2176.

Nuss, W., 1989: Air-sea interaction on the structure and intensification of an idealized marine cyclone. *Mon. Wea. Rev.,* **117,** 351–369.

——, and R. A. Anthes, 1987: A numerical investigation of low-level processes in rapid cyclogenesis. *Mon. Wea. Rev.,* **115,** 2728–2743.

O'Brien, E. W., and E. P. Chassignet, 1995: Extratropical large-scale air-sea interaction in a coupled and uncoupled ocean–atmosphere model. *Climate Dyn.,* **12,** 53–65.

Palmer, T. N., and Z. Sun, 1985: A modelling and observational study of the relationship between sea surface temperature in the north-west Atlantic and the atmospheric general circulation. *Quart. J. Roy. Meteor. Soc.,* **111,** 947–975.

Petterssen, S., D. L. Bradbury, and K. Pedersen, 1962: The Norwegian clone models in relation to heat and cold sources. *Geofys. Publ.,* **24,** 243–280.

Polonsky, A. B., S. A. Baev, and A. Diakite, 1992: On the response of the ocean upper layer to synoptic variability of the atmosphere. *Dyn. Atmos. Oceans,* **16,** 225–248.

Reed, R. J., and A. J. Simmons, 1991: An explosively deepening cyclone that was unaffected by concurrent surface energy fluxes. *Wea. Forecasting,* **6,** 117–122.

Sanders, F., 1986: Explosive cyclogenisis in the west central North Atlantic Ocean, 1981–84. Part I: Composite structure and mean behavior. *Mon. Wea. Rev.,* **114,** 1781–1794.

——, and J. R. Gyakum, 1980: Synoptic-dynamic climatology of a bomb. *Mon. Wea. Rev.*, **108,** 1589–1606.

Ting, M., and S. Peng, 1995: Dynamics of early and midwinter responses to the northwest Atlantic SST anomalies. *J. Climate,* **8,** 2239–2254.

Uccellini, L. W., R. A. Petersen, K. F. Brill, P. J. Kocin, and J. J. Tuccillo, 1987: Synergistic interactions between an upper-level jet streak and diabatic processes that influence the development of a low-level jet and a secondary coastal cyclone. *Mon. Wea. Rev.*, **115,** 2227–2261.

Wallace, J. M., G.-H. Lim, and M. L. Blackmon, 1988: Relationship between cyclone tracks, anticyclone tracks, and baroclinic wave guides. *J. Atmos. Sci.,* **45,** 439–462.

Whitaker, J. S., and R. M. Dole, 1995: Organization of storm tracks in zonally varying flows. *J. Atmos. Sci.,* **52,** 1178–1191.

Whittaker, L. M., and L. H. Horn, 1983: Extratropical cyclone activity for four midseason months. *J. Climatol.,* **4,** 297–310.

Zhao, Y. P., and G. A. McBean, 1986: Annual and interannual variability of the North Pacific ocean–atmosphere total heat transfer. *Atmos.–Ocean,* **24,** 283–291.

Zorita, E., V. Kharin, and H. von Storch, 1992: The atmospheric circulation and sea surface temperature in the North Atlantic area in winter: Their interaction and relevance for Iberian precipitation. *J. Climate,* **5,** 1097–1108.